CrossMark

ORIGINAL ARTICLE

Hyper-velocity impact risk assessment and mitigation strategies in the context of future X-ray astronomy missions

Emanuele Perinati[1] · Martin Rott[2] ·
Andrea Santangelo[1] · Chris Tenzer[1]

Abstract Future X-ray astronomy missions will be based on instruments with apertures much larger than those used up to now. Therefore, the risk posed by hyper-velocity dust grains in the space environment to the onboard instrumentation will increase, especially when a larger aperture is combined with a longer focal length. Starting from the lessons learned from the XMM and Swift satellites, we review the question of hyper-velocity impacts and discuss the expected impact-rate, risk of damage and possible mitigation strategies in the context of LOFT, eROSITA and ATHENA.

Keywords X-ray astronomy · micrometeoroids · orbital debris · dust accelerators · Whipple shield · ESABASE2

1 Introduction

Our solar system is filled with space dust, both meteoroids and debris, whose typical size lies in a range from less than 1 μm to above 1 cm. Meteoroids are natural interplanetary mineral grains, most of which are believed to originate from collisions between asteroids and venting from comets. Dust fragments produced by artificial objects placed in orbit are referred to as orbital debris. In the vicinity of the Earth, meteoroids and debris have average velocities relative to a spacecraft in orbit of ~

✉ Emanuele Perinati
emanuele.perinati@uni-tuebingen.de

[1] IAAT - Institut für Astronomie und Astrophysik, Universität Tübingen, 72076 Tübingen, Germany

[2] LRT - Lehrstuhl für Raumfahrttechnik, Technische Universität München, 85748 Garching, Germany

🙏 Springer

20 km/s and ~10 km/s, respectively. Therefore, dust impacts represent a potential threat for space-borne instruments, due to the structural damages they can cause, which in turn may imply degradation of the performance or even, in the worst case, the failure of the instruments. As an example, both the MOS and pn cameras on board the X-ray Multi Mirror (XMM) satellite suffered a number of impacts, which caused significant damages [1] and even the failure and loss of CCD # 6 (on 9 March 2005) and CCD # 3 (on 11 December 2012), both belonging to MOS1; on 27 May 2005 an impact caused a severe damage to the MOS CCD of the X-Ray Telescope on board Swift, which resulted in the inability to operate in all modes [2]. In these cases, it was believed that hyper-velocity dust grains entered the field of view (FOV) of the telescope being focussed by the mirror shells or being fragmented after impacting against them, generating a spray of secondary fragments, some of which were scattered down to the focal plane. In unfocussed instruments the resulting damage may be even more serious, as dust grains can reach the detectors more easily without any loss of kinetic energy. The assessment of the impact risk is crucial to estimate the probability of damages, quantify the degradation of the instrumental performance, and possibly identify and implement suitable shielding solutions. In this article we review and summarize the results of an impact risk assessment conducted for the LOFT, eROSITA and ATHENA space missions.

2 Hyper-velocity impacts

Meteoroids smaller than 100 μm are usually called micrometeoroids and constitute, in number, more than 99% of all meteoroids. The precession of a satellite orbit and the tilt of the Earth equatorial plane with respect to the ecliptic plane implies that the flux of micrometeoroids can be assumed isotropic relative to Earth. According to [3], the smallest micrometeoroids (< 10 μm) include iron grains (~ 46%), silicate grains (~ 17%) and grains made of a lower density material (~ 37%). Most micrometeoroids larger than 10 μm are expected to be silicate grains with an average density of ~2.5 g/cm^3. On the other hand, orbital debris consists of fragments of various size left in the space environment by spacecrafts and artificial satellites. Unlike micrometeoroids, debris is not isotropically distributed and its flux depends on the altitude and inclination of the orbit, with low Earth highly inclined orbits usually presenting a higher concentration of debris. Furthermore, along an orbit the concentration of debris can be strongly dependent on the direction of observation. The smallest debris (< 20 μm) includes mostly alumina grains generated when solid rocket motors burn out, while at larger size paint flakes, slag particles and fragments produced by collisions of bigger spacecraft parts are abundant. Figure 1 shows the expected fluence of micrometeoroids and debris in the LOFT orbit, according to the cumulative populations reported in [4].

When a hyper-velocity grain impacts on a target, the resulting structural damage is the formation of a crater on its surface (or a clear hole in case the impactor has enough energy to fully penetrate through the target). Typically, at a speed exceeding a few kilometers per second the process is hydrodynamic: the impact point becomes a hot spot and the target behaves like a fluid, with the damage propagating through it as a shock wave. The high temperature produces a partial vaporization of the impactor with associated ionization and formation of a plasma cloud rapidly expanding from the
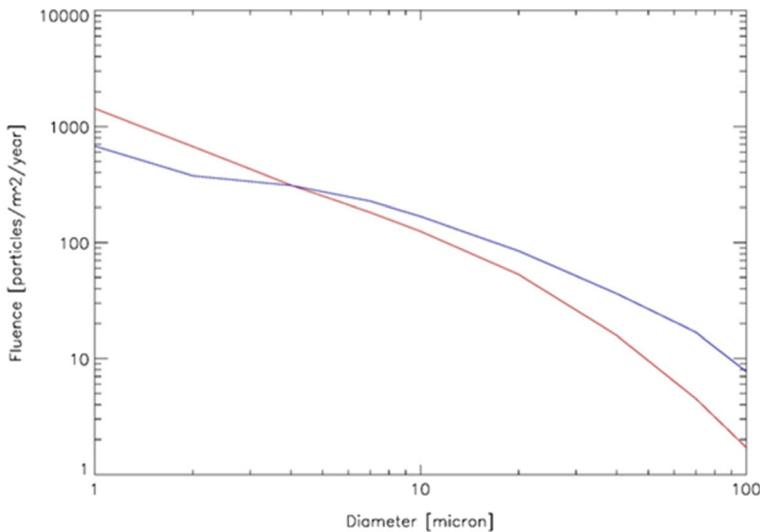
Fig. 1 Average cumulative fluence of micrometeoroids (red curve) and debris (blue curve) expected for a randomly oriented plate in the LOFT orbit [4]

impact point. This plasma cloud plays an important role in hyper-velocity experiments both on ground and in space, in fact placing an electric field around the target it is possible to collect separately electrons and ions in the plasma cloud generated by an impact and obtain two pulse signals whose characteristic parameters are related to the characteristics of the impactor. The morphology of the crater is somehow different for ductile and brittle materials: in the first case the crater is usually nearly spherical, while in the second case typically an inner crater with smaller diameter forms within a larger outer crater. The damage equation allows to predict the crater size and depth as a function of a number of parameters. For single-wall targets the general equation for the crater depth (p) is [5]:

$$p = c \cdot d_p^{\alpha \cdot} v_p^{\beta \cdot} \rho_p^{\gamma \cdot} \rho_t^{\delta \cdot} \cos^{\varepsilon} \Theta \tag{1}$$

where d_p, v_p and ρ_p are diameter, velocity and density of the impacting particle, Θ is the angle of incidence, ρ_t is the density of the target, and c is a characteristic constant. This empirical formula has a general validity, however the values of the parameters $\alpha, \beta, \gamma, \delta$ and ξ are different for ductile and brittle materials and also may change depending on the range of the variables. Equation (1) and commonly used values of the parameters are reported in ESABASE2.

3 Impact risk assessment for LOFT

The *Large Observatory For X-ray Timing* [6] is a medium-class space project proposed as part of the ESA Cosmic Vision program. In 2011 it was selected by ESA as one of the candidates for the M3 launch in 2022–2024, with a nominal duration of 3 (+2) years. It would be placed in a low Earth near-equatorial orbit (inclination <5°) at ~600 km altitude.

The scientific goal of LOFT is the investigation of the strong-field gravity and the equation of state of ultra-dense matter, through the observation at high count-rate of compact objects in the 2 to 30 keV energy band with an unprecedented effective area (~ 10 m^2 @8 keV). The adopted innovative technology relies on the use of Silicon Drift Detectors (SDDs) derived from those developed by INFN for the ALICE experiment at LHC/CERN. Each SDD tile is a 450 μm thick fully depleted silicon wafer with a quite large size (10 × 7 cm^2) and capable of achieving high temporal resolution (~7 μsec) combined with good spectral resolution (< 260 eV FWHM). A system of cathodes implanted at the surface, on both sides, provides a potential varying from the center of the detector towards the two opposite edges, allowing for a drift of the charges generated by the absorbed photons towards a set of collecting anodes (Figure 2).

There are two instruments onboard LOFT (Figure 3): the *Large Area Detector* (LAD) [7] and the *Wide Field Monitor* (WFM) [8]. In the design proposed by the Consortium, the LAD features a large geometric area of ~15 m^2 achieved by assembling 2016 SDD tiles into 126 individual modules (4 × 4 tiles each) divided on 6 panels (3 × 7 modules each). Different configurations based on a smaller number of panels have been investigated as well. The LAD is a collimated experiment and the 6 mm thick micro-pore glass collimator on top of the SDD assembly has a FOV ~ 10^{-4}π. The WFM consists of 10 cameras divided in 5 pairs, each camera is a coded-mask experiment with 4 SDD tiles in the detection plane. The WFM has an entrance area of ~0.7 m^2 and a large FOV of ~5.5 sr (at zero-response), useful for long term monitoring of variable sources.

The expected effect of hyper-velocity impacts on the SDD tiles onboard LOFT is a permanent increase of the anode leakage current, and a possible alteration of the electric field at the surface caused by craters. In the following Section 3.1 and Section 3.2 we present the impact risk assessment separately for the WFM and the LAD.

3.1 Impact risk assessment for the LOFT/WFM

Each WFM camera has a tungsten-based coded-mask with a geometric area A ~ 0.07 m^2 and a zero-response FOV ~ 0.8·π. The open fraction is OF = 0.25. The number of impacts n$_{imp}$ at the end of the mission is calculated as:

$$n_{imp} = F \cdot A \cdot OF \cdot FOV \cdot T / 2\pi \qquad (2)$$
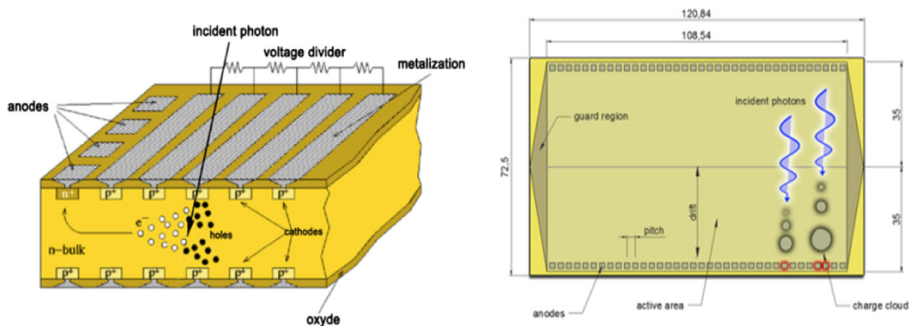

Fig. 2 Schematic of the SDD used for LOFT (image credits: LOFT Consortium). The reported dimensions are typical values of the prototypes produced up to now
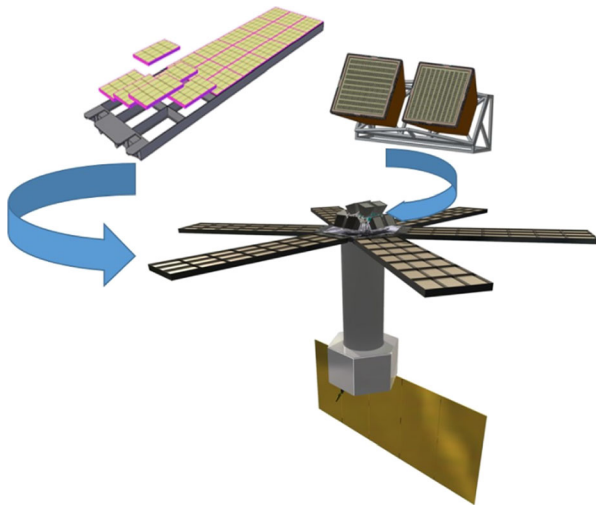
Fig. 3 The LOFT geometry with the 6 LAD panels and the 10 WFM cameras on top. LAD unit: 1 panel = 21 modules = 16 × 21 SDDs; WFM unit: 2 cameras = 4 × 2 SDDs (image credits: LOFT Consortium)

where F is the dust flux and T is the duration of the mission. We do not take into account possible stray-dust that may reach the SDDs from outside the FOV, after impacting on the coded-mask walls. We report in Table 1 the average number of impacts by micrometeoroids and debris in 5 years resulting from (2).

For each camera, in 5 years we expect a number of impacts by dust grains smaller than 10 μm between ~50 and ~80, and a number of impacts by dust grains in the range 10 μm to 100 μm between ~5 and ~20, to a 0.9 confidence level. Therefore, assuming a Poisson distribution of the events and considering that according to simulations grains up to ~10 μm size would likely be stopped by the combined effect of the ~8 μm thick kapton optical and thermal filter, mounted on the coded-mask, and the silicon oxide passivation layer on top of the SDD depleted volume, an average value of ~10 impacts for each single WFM camera should be expected, which corresponds to a probability of ~99% that all four SDDs suffer some damage in 5 years in orbit. Clearly this risk is unacceptable and additional shielding is required to mitigate it.

Table 1 Average number of meteoroids and orbital debris of different size expected for each single WFM camera in 5 years. We assumed a geometric area A = 0.07 m^2 (with an open fraction OF = 0.25) and a FOV = 0.8·π

Particle size	Meteoroids in 5 years	Debris in 5 years
1–10 μm	~46	~18
10–50 μm	~4	~6
50–100 μm	~0.3	~0.7
>100 μm	~0.06	~0.3

3.1.1 Shield design

The shield for the WFM should be able to stop hyper-velocity grains up to ~100 μm size. This may be achieved with a Whipple configuration (Figure 4), using an outer layer (acting as a bumper) plus an inner layer (acting as a rear-wall) made of a material capable to withstand hyper-velocity impacts placed at a certain distance behind the bumper. The bumper is expected to shock the primary grains, converting part of their kinetic energy into heat, which results in an explosive fragmentation producing a spray of much smaller secondary grains. Such cloud of secondary, less energetic, fragments emerging from the bumper has then to be fully absorbed in the rear-wall layer. For the WFM, the challenge is to obtain the desired performance with layers as thin as possible, in order to minimize the impact on the quantum efficiency of the instrument. The distance between the two layers is approximately 20 cm, corresponding in the current baseline geometry to the distance between the coded-mask and the detector plane.

The bumper for the WFM would consist of a layer of kapton ~8 μm thick, which is already envisaged in the WFM design as an optical and thermal filter. For the rear-wall, we selected polypropylene, which provides a high mechanical resistance and guarantees sufficient X-ray trasmissivity (at least ~70% @2 keV is required) across the entire WFM energy band. As there is a lack of experimental data about the response of thin plastic layers to hyper-velocity impacts, we considered it necessary to perform a laboratory test of the shield concept described above.

3.1.2 Hyper-velocity test campaign at TUM

A hyper-velocity impact test campaign was conducted at the plasma accelerator of the Technical University of Munich (TUM) [9]. Figure 5 shows a schematic of the accelerator. The discharge of a 16 kV capacitor bank through ignitron switches into a
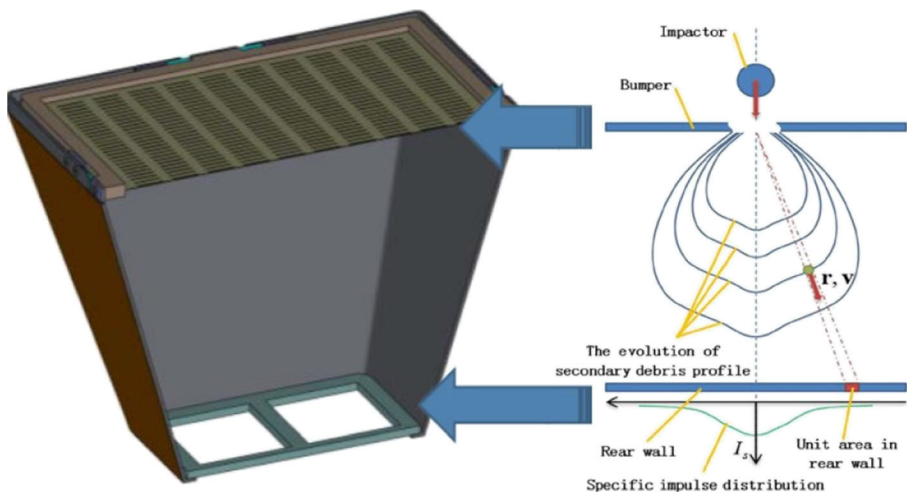

Fig. 4 A Whipple shield consist of an outer bumper and a rear-wall placed at a certain distance from it. The bumper should produce fragmentation of the primary impacting grains, the spray of smaller less energetic secondary fragments is then stopped by the rear-wall. Arrows indicate where the bumper and rear-wall layers would be placed in each WFM camera (half camera is shown here)
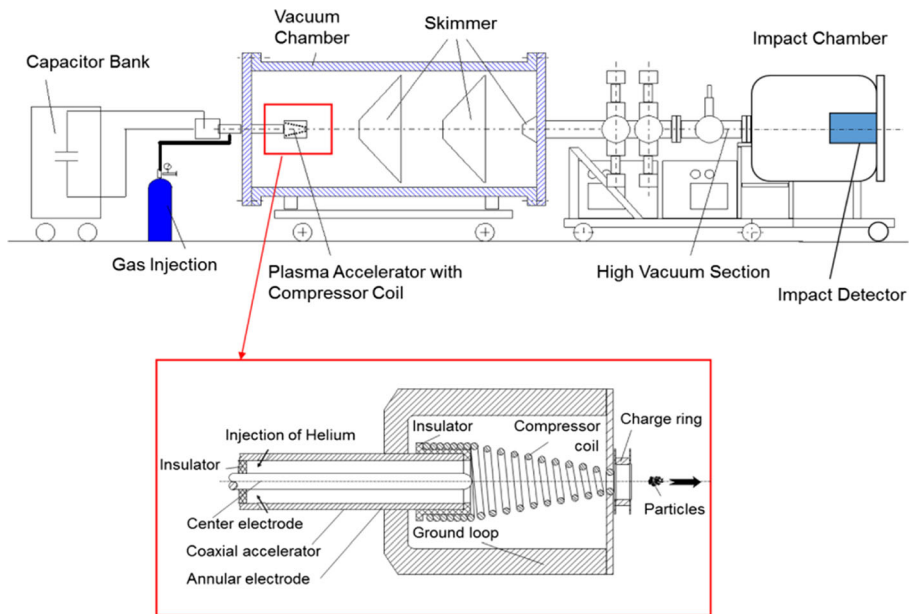
Fig. 5 Schematic of the plasma accelerator at TUM (image credits: M. Rott)

plasma gun filled with a few cm^3 of helium gas generates a plasma, which is accelerated along the coaxial electrodes by electrical currents and magnetic fields. The plasma reaches the compressor coil at ~80 km/s, where the flow is compressed and the grains exposed to the flow pressure are drag accelerated. This machine is unique in the generation of hyper-velocity grains of intermediate size, as Van de Graaff accelerators can accelerate only smaller grains of a few micron size and light gas guns usually work with grains larger than 100 μm. The typical particle distribution achievable at TUM is in a range of size from ~10 μm to ~100 μm. The chemical species used in the accelerator is silicate with a density of ~2.5 g/cm^3, which is expected to simulate well most of the larger micrometeoroids and orbital debris. The accelerated grains impact the target at nearly vertical incidence. This represents a conservative simulation of the orbital case, as in space oblique impacts, which are expected to cause less damage than vertical ones, are more probable due to the large FOV of the WFM cameras.

We built several individual targets with the same specifications in order to shoot only few particles against each one, for an easier inspection of the layers in the optical microscope after the bombardment. Each target is a shield sample made of a layer of kapton ~8 μm thick coupled to a layer of polypropylene ~ 15 μm thick. To exploit the mechanical mounting that was already existing at the accelerator we placed the kapton bumper and the polypropylene rear-wall at 4.5 cm distance from each other, the largest possible value allowed in the configuration of the chamber (Figure 6). This spacing is smaller than the actual distance exploitable on the WFM, i. e. our experimental configuration was actually less effective and the results of the test can be assumed as a conservative case. A possible issue was how to get a clear understanding of the results of the test, as it would have been difficult to look in the microscope for the very small
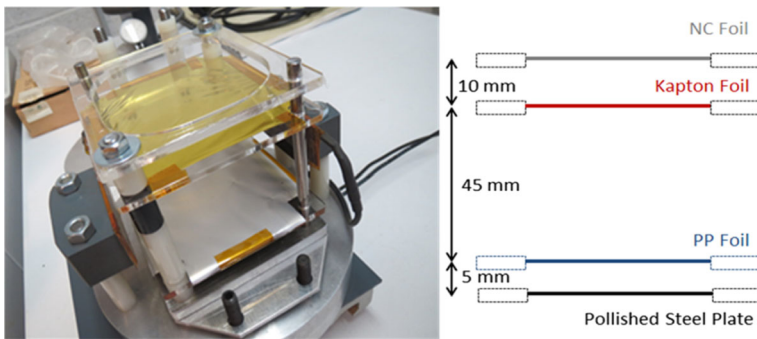
Fig. 6 The shield target: all layers are fixed to plastic supporting frames 9 × 8 cm². At the two sides of the target the two charge collecting plates are visible

craters or holes produced by tiny secondary fragments and distinguish them from possible defects and impurities on the unpolished polypropylene surface. To make the inspection easier and faster, we plated the polypropylene layers with 150 nm aluminum. This allows to easily locate and recognize the pattern of tiny imprints created by the spray of secondary impacting fragments, as the aluminum coating makes the layer opaque to the visible light, but in the impact points the fragments remove the metal and the layer becomes transparent. By illuminating it from the uncoated backside with a laser beam or a lamp, it is then possible to see clearly the pattern produced by impacts (Figs. 8 and 9). Eventually, a polished steel plate is placed behind the rear-wall to detect possible imprints left by ejecta emerging from the polypropylene layer as a proof of rear-wall perforation. We applied the same aluminum coating also to the kapton layers, as the presence of metal helps to get enough charge generation during the bombardment for triggering the detection of the impacts. As the applied coating is much thinner than the layer thickness and grain size, we assume that it did not have any influence on the dynamics of the impacts and did not alter the result.

Ultrafast drag acceleration leads to ablation and deflection of the grains, therefore it is not possible to select size, speed and impact point prior to a shot, instead the impact parameters are measured after each shot. Figure 7 explains the details of the procedure: two charge collector plates are mounted at the side of the target, the detection of a charge signal by these plates gives information that an impact occurred. Relating the time of this trigger signal with the time of the capacitor discharge makes it possible to estimate the speed of the grains, as the distance between the compression coil and the target is known (4.5 m). There is a short delay between the capacitor discharging time and the actual time the grains leave the coil, which from previous tests was estimated ~20 μsec, on average. As all grains produced by the accelerator need at least ~450 μsec to cover the distance between the coil and the target, an error of ~20 μsec corresponds to an accuracy in the estimate of their speed better than 10%. A special nanocrystalline thin film (100 nm thick) is mounted in front of the target, the impacting grains pass through it without any fragmentation and form well defined clear holes. Measuring the size of the holes in the optical microscope gives precisely the size of the grains impacting the target. The precision in determining the diameter of the holes is ~1 μm, however in some cases the hole may not be perfectly round, depending on the actual shape of the particle at the impact point, in such cases the hole size is estimated by some other criterion considering the actual shape of the hole in the x,y plane. Since in our setup the
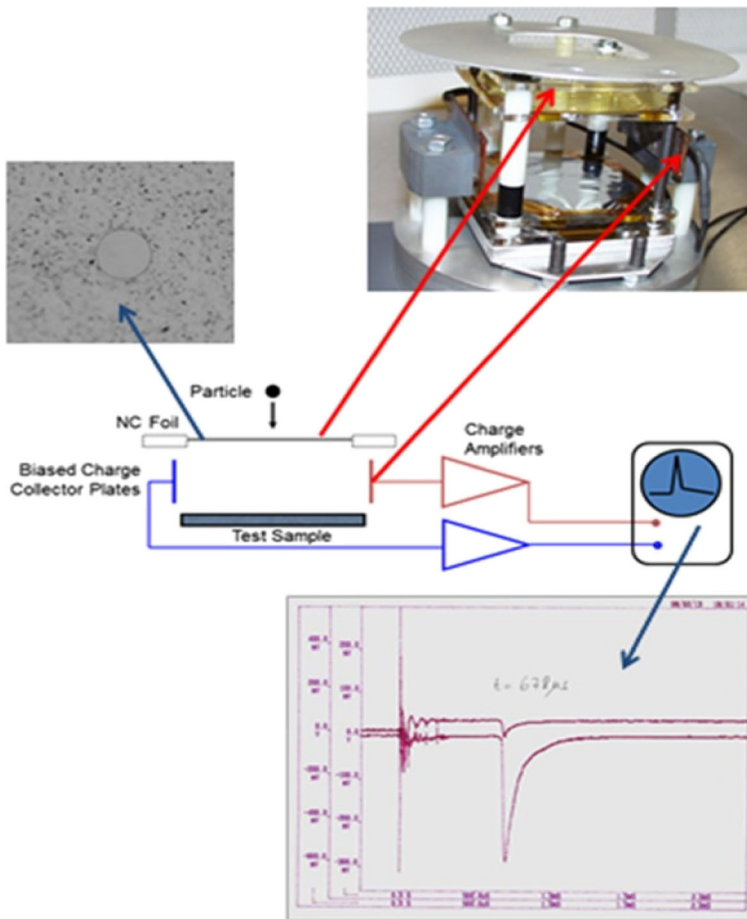
Fig. 7 The measurement of the impact parameters: the impactor size is measured from the hole created in the nanocrystalline foil. The strong signal at $t = 0$ corresponds to the discharge of the capacitot bank. The time of the impact is given by the charge signal. The impact speed is derived from a measurement of the time of flight

impacting grains leave the largest holes on the kapton layer, the location of the impacts is determined by inspecting at first this layer in the microscope. Then, the position of a hole on the kapton layer indicates the position on the nanocrystalline foil where the clear hole will be found and restricts as well the area on the polypropylene layer for the search for holes or craters left by secondary fragments. Finally, the position of the area affected by the secondary spray on the polypropylene layer localizes the area on the polished steel plate for the search for tiny imprints of possible ejecta indicating whether perforation of the polypropylene occurred or not.

During the test campaign we have performed 13 shots for the combination kapton (bumper) 8 μm + polypropylene (rear-wall) 15 μm. It is worth stressing that the number of shots is constrained by the long time required for the proper setting of the accelerator as well as the high costs of running it. In general, a whole day is needed to obtain a single useful shot (i.e. a hit on the target), moreover it was necessary to open the chamber after each impact breaking the vacuum in order to remove the target and

perform inspection of the bombarded target in the microscope. However, the achieved statistics was enough to understand the physical processes and the response of the shield to hyper-velocity impacts. In fact, we observed three regimes of velocity, each associated with a typical behaviour of the grains hitting the kapton bumper:

a) v > 7 km/s: grains undergo a complete explosive fragmentation or even evaporation (the smallest ones), producing spray of tiny secondary fragments which are then stopped by the polypropylene rear-wall (Figure 8);
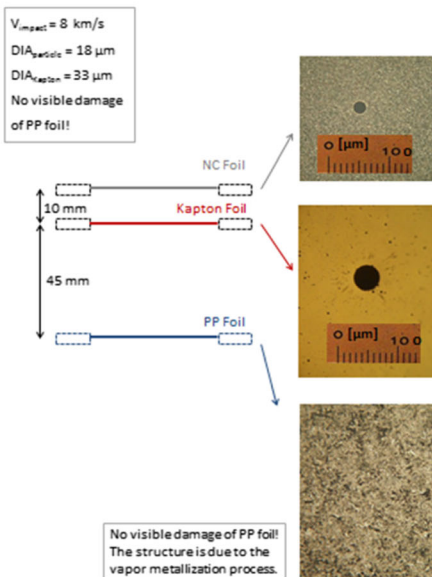
b) 5 km/s < v < 7 km/s: grains undergo a partial fragmentation, resulting in a number of smaller grains some of which are still big enough to make clear holes in the polypropylene rear-wall (Figure 9);

c) v < 5 km/s: grains do not undergo fragmentation and perforate both layers (Figure 9).

Figures 8 and 9 have been selected as typical examples that illustrate the scenario described above, the photographs were taken during inspection of the bombarded layers at the microscope. We compared our results with the predictions of the double wall shield model described by eq. (3), applied to our configuration using the set of parameters reported in Table 2 (the so-called International Space Station (ISS) configuration in ESABASE2) and have found that they are in a remarkable good agreement, as shown in Fig. 10.

$$d(v_p) = \left(\frac{t_b + K_2 \cdot t_s^{\mu} \cdot \rho_s^{v2}}{K_1 \cdot \rho_p^{\beta} \cdot v_p \gamma \cdot \rho_b^{k} \cdot s^{\delta} \cdot \rho_s^{v1}} \right)^{\frac{1}{\lambda}} \tag{3}$$
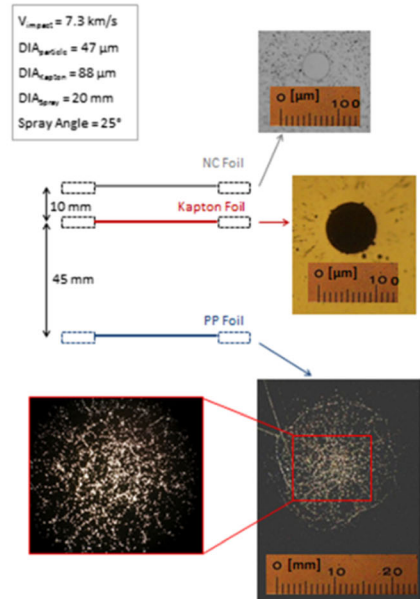

Fig. 8 Typical impacts at high velocity: (*left*) the primary grain has a small size and is evaporated by the kapton bumper, no solid fragments emerge; (*right*) the primary grain has a large size and is completely fragmented by the kapton bumper producing a spray of secondary tiny (micron and sub-micron sized) fragments fully stopped by the polypropylene rear-wall
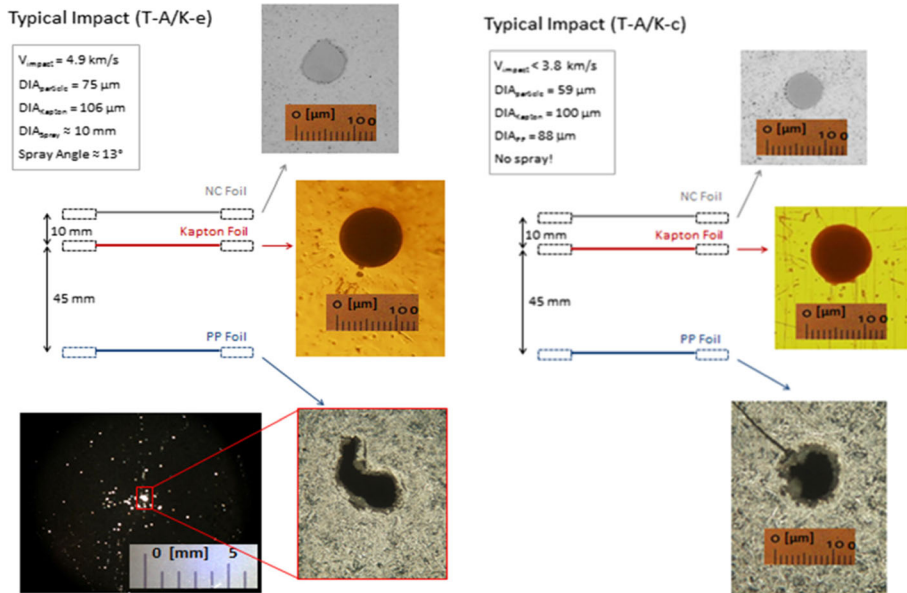
Fig. 9 *Left:* Typical impact at medium velocity: the primary grain is partially fragmented by the kapton bumper into a certain number of secondary smaller fragments, some of them are still big enough to make holes in the polypropylene rear-wall (notice that the size of the holes in the photograph appear magnified with respect to the actual one due to the fact that the impacting fragments remove some metallization also around the holes). *Right:* Typical impact at low velocity: the primary grain is not fragmented by the kapton bumper and it perforates also the polypropylene rear-wall

In eq. (3) v_p is the grain speed and d is the critical grain size, i.e. the largest size the shield would be able to withstand at a given speed; t_s and t_b are the thicknesses of bumper and rear-wall, respectively; ρ_p and ρ_s are the densities of grain and rear-wall, respectively; s is the spacing between bumper and rear-wall. The values of the parameters vary depending on the range of speed, as reported in Table 2.

We could not validate the model predictions for grains larger than ~70 μm and faster than ~7 km/s, as this is close to the limit of the accelerator. However, the good

Table 2 Values of the parameters to be used to predict the critical grain size at a given speed according to the ISS double wall shield model. The parameters K_1 and K_2 depemd on σ (expressed in ksi units), that is the rear-wall stress yield (in our application we assumed σ ~7 ksi)

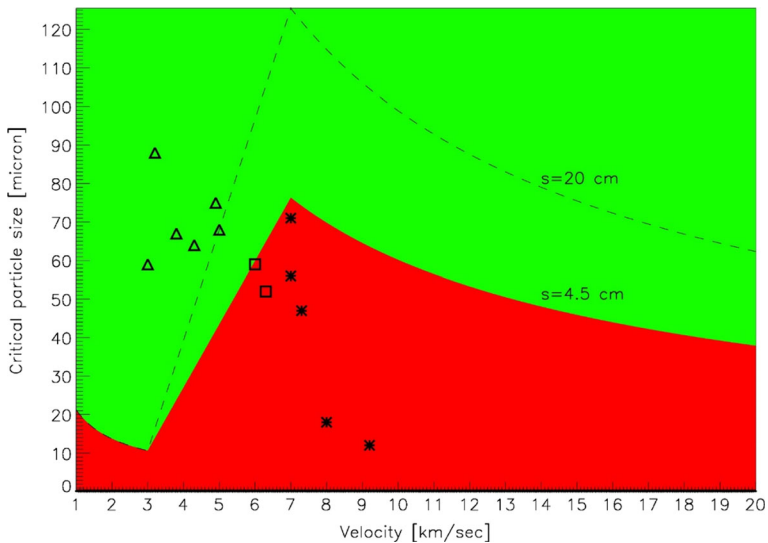| v < 3 km/s	v > 7 km/s
$K_1 = 0.6 \cdot (\sigma/40)^{-1/2}$, $K_2 = (\sigma/40)^{-1/2}$	$K_1 = (3.918 \cdot (\sigma/70)^{1/3})^{-1/2}$, $K_2 = 0$
$\mu = 1$	$\mu = 0$
$\beta = 1/2$	$\beta = 1/2$
$\gamma = 2/3$	$\gamma = 1$
$k = 0$	$k = 0$
$\delta = 0$	$\delta = -1/2$
v1 = 0, v2 = 0	v1 = 0.167, v2 = 0

Fig. 10 Simulated performance of our kapton + polypropylene shield by adopting the ISS model described by eq. (3) assuming a linear interpolation between 3 km/s and 7 km/s: the red area indicates stopped grains, i.e. the combination of parameters for which the shield is effective; the green area indicates grains passing through, i.e. shield failure. The points are experimental data of shots performed in the test campaign at TUM: * = shield effective (polypropylene was not perforated); □ = unclear case (polypropylene was perforated but no impact imprints were detected on the polished steel plate below it, possible complete evaporation of the ejecta by polypropylene); ∆ = shield failure (polypropylene was clearly perforated). In the simulation we assumed ~7 ksi as the stress yield of polypropylene, the point P = (~ 7 km/s, ~ 70 μm) demonstrates that the actual stress yield of our polypropylene sample may be larger than 7 ksi but it should not be much lower. The simulation considers vertical incidence of the grains. The dashed line is a simulation showing where the red area would extend by increasing the spacing between bumper and rear-wall from 4.5 to 20 cm, as in the actual WFM configuration: a larger spacing allows for a larger opening of the spray cone emitted by the kapton bumper, resulting in the momentum of the secondary fragments impinging onto the polypropylene rear-wall being distributed over a wider area, then producing a lesser amount of damage

agreement in the achievable range of parameters suggests that the model predictions should be expected consistent in different ranges of the parameters as well. Therefore, as shown in Fig. 10 for a configuration with 20 cm spacing we assume that the shield would be able to stop grains up to ~100 μm at 10 km/s, and grains up to ~60 μm at 20 km/s. As ~0.2 impacts by meteoroids larger than 60 μm and ~0.3 impacts by debris larger than 100 μm are expected in 5 years in orbit, we calculate a probability of ~60% of having no impacts in 5 years, assuming a worst case vertical impact occurrence. Considering that within an acceptance angle of 0.8·π oblique incidence is more probable than vertical incidence, the actual picture seems even more favorable, e.g. at 30° incidence the probability of no impacts can be expected higher than 85%.

3.2 Impact risk assessment for the LOFT/LAD

Despite the huge geometric area of 15 m^2, the relatively small FOV ($10^{-4}\pi$) of the LAD restricts the risk of impact only to grains with size less than a few micron, the most abundant ones in the environment. Taking into account both micrometeoroids and orbital debris the resulting average rate is ~5 impacts in

5 years by grains smaller than 10 μm. However, an optical/thermal filter made of a foil of kapton 1 μm thick plated with 40 nm Al on both sides is envisaged in the baseline configuration of the LAD. This filter can be mounted above or below the collimator, and the first option would be preferable in terms of protection of the SDDs from impacts. In fact, the combination of kapton and silicon oxide actually works as a double-wall shield with 6 mm spacing. We estimated the shielding effectiveness of this double-wall using the ISS model, assuming 1 μm thick passivation. According to our simulations micrometeoroids smaller than ~3 μm and debris smaller than ~5 μm would not be able to reach the active region below the passivation. Therefore, the average number of hazardous impacts over 5 years in orbit is reduced to ~1. Assuming a Poisson distribution of the events and considering that the LAD is composed by 2016 independent tiles, an average rate of 1 event corresponds to a probability of ~37% that the effective area of the LAD is degraded by 0.05% in 5 years in orbit, a probability of ~19% that it is degraded by 0.1% and virtually zero probability that it is degraded by more than 1%. Then, even in the worst case, i.e. assuming that each impact implies a complete failure of the hit tile, this scenario is indeed not concerning. Furthermore, we characterized the response of SDD prototypes to impacts, performing hyper-velocity impact tests at the dust accelerator of the Max-Planck Institute for Nuclear Physics (MPIK) in Heidelberg to quantify to what extent the detector functionality would be degraded by impacts. A detailed discussion of the results of these measurements can be found in [10]. In summary, the laboratory tests evidenced the robustness of the SDD in the range of impact parameters expected for the LAD. Figure 11 reports an example of what typically happens in the case of impacts that produce craters deep enough to reach the depleted bulk: the level of leakage current of the SDD undergoes a small step of increase as a consequence of each impacting grain penetrating through the passivation layer. Since impacts produce permanent damages, after a step of increase the leakage current does not recover back to the previous value.
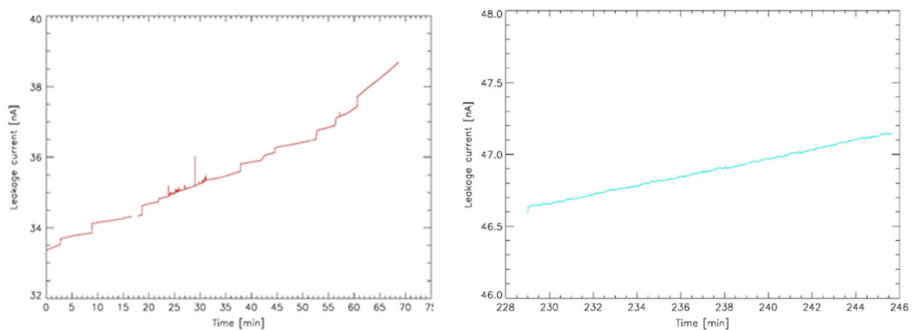

Fig. 11 Some results from the impact test campaign conducted on an SDD prototype at MPIK. *Left*: variation of the SDD leakage current under bombardment with iron grains of ~2 μm size at ~2 km/s, which are expected to have enough penetration to reach the depleted volume below the passivation. Each impact produces a small step of the overall leakage current (in this test all anodes were bonded together). *Right*: no signals are detected from smaller grains unable to reach the depleted volume

4 Impact risk assessment for eROSITA

The *extended ROengten Survey Imaging Telescope Array* [11] is a German X-ray instrument to be flown in 2018 onboard the Russian *Spectrum Roentgen Gamma* space mission. It consists of seven identical and coaxial Wolter-I telescopes coupled to seven identical pnCCD cameras at the focal plane. As experienced by XMM, also for eROSITA it is expected that hyper-velocity dust grains may be scattered off the mirror shells down to the focal plane. Therefore, we simulated the dust stopping power for the two possible filter configurations adopted on eROSITA using the ISS model in ESABASE2. We compared the difference in performance of a single filter made of 200 nm polyimide coated with 100 nm aluminum and a double filter consisting of a foil of 200 nm polyimide plus a foil of 200 nm aluminum separated by 6 cm (Fig. 12). In the first case, the filter is able to withstand only impacts by grains smaller than about 200 nm (at 1 km/s), which may be representative of secondary fragments scattered to the focal plane after an initial fragmentation against the mirror shells of primary grains with larger size and higher velocity. Fragments larger than 200 nm would perforate the filter reaching the detector surface. In the second case, the performance is enhanced for impacting grains with higher velocity, enabling fragmentation onto the polyimide and subsequent reabsorption in the aluminum foil of the ejected smaller fragments. However, slower fragments would still pass through, as they do not have sufficient energy to explode after impacting the polyimide. The red area in Figure 12 indicates which grains would be stopped by the shield, thus the simulation suggests that having two filters separated by 6 cm gives a significant advantage, reducing the impact risk by faster fragments. However, it is worth stressing that the ISS model, as well as other similar models developed to describe the behavior of a multi-layer shield, was derived and validated in quite different conditions, i.e. metal layers and larger thicknesses. Therefore, its predictions in case of very thin plastic filters may not be completely reliable. We performed a very preliminary test at the dust accelerator of the Max-Planck Institute for Nuclear Physics (MPIK) in Heidelberg using the smaller test chamber available at the facility, that is a flange provided with a collimator enclosed in a cylindrical case. The case has a 1 cm diameter hole on the top allowing for the passage of hyper-velocity
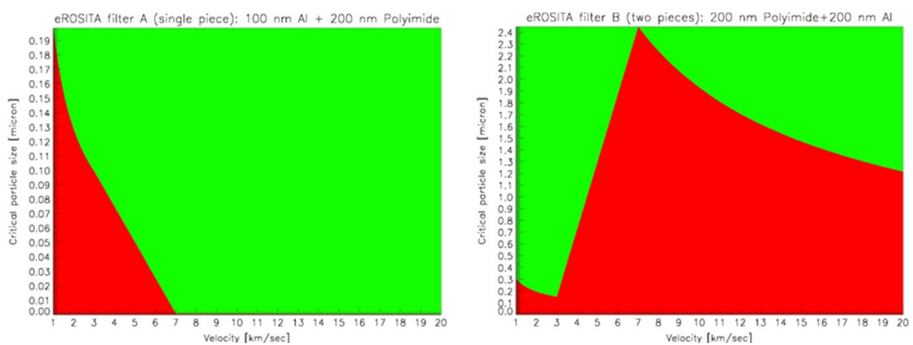

Fig. 12 *Left:* the dust stopping power of a filter consisting of 200 nm polyimide coated with 100 nm Al simulated using the ISS model: the area in red indicates grains (velocity, diameter) that would be stopped by the filter. *Right:* the same simulation for a two-pieces filter made of 200 nm polyimide and 200 nm aluminum placed at 6 cm distance from each other, in this case the filter is capable of stopping grains up to 1–2 μm at high speed
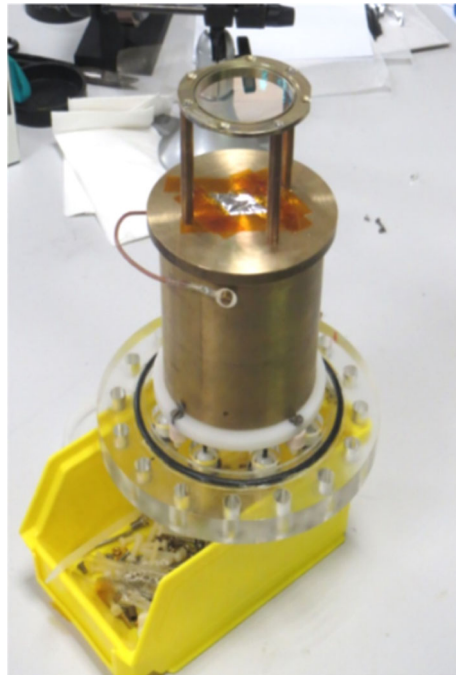
Fig. 13 The experimental setup used to test the response to hyper-velocity impacts of the eROSITA optical blocking filter, mounted on a cylindrical case which works as an induction tube to monitor the passage of hyper-velocity charged grains inside. The flange is then fixed at the end of the beamline

grains through the collimator. Behind the collimator there is a supporting plate on which usually the targets are mounted. However, we mounted externally our target (the polyimide filter) at 6 cm distance from the top of the flange to simulate the actual filter-wheel configuration (Figure 13). A foil of Al 400 nm thick was used to close the entrance hole of the flange. This is twice the thickness of the aluminum plating on top of the pnCCD, the reason for using 400 nm instead of 200 nm is simply that 400 nm was the thinnest thickness available on the market. However, the choice is acceptable as the stopping power of this Whipple configuration is expected quite similar to that with a 200 nm foil. The flange was mounted in the beamline. Dust grains get positively charged before shooting, so that passing through the collimator they induce a charge distribution, which is amplified and monitored by a sensitive detector. Therefore, we used the signals from the collimator as an alert confirming that grains or secondary fragments ejected by the filter penetrated also the aluminum foil.

Figure 14 shows the typical distribution achievable with the dust accelerator at MPIK. We selected grains in the range of size between 200 and 500 nm, and performed three sets of measurements:

a) in the first case we selected a speed in the range between 2 and 3 km/s and bombarded directly the aluminum foil. For all shots, a signal from the collimator was recorded, meaning that all grains perforated the foil; b) in the second case we mounted the polyimide filter at 6 cm from the aluminum foil and bombarded it with grains with a speed in the same range between 2 and 3 km/s. Also in this case, we recorded signals
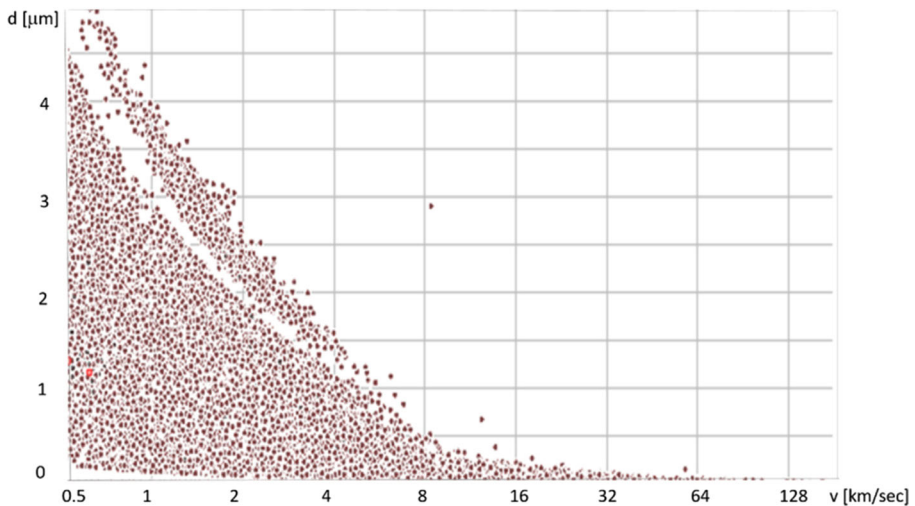
Fig. 14 Typical grain distribution achievable with the dust accelerator at MPIK

from the collimator, meaning that such particles penetrated through both the polyimide and the aluminum foil, in accord with the model prediction c) in the third case we increased the speed to values between 6 and 8 km/s. Even in this case, we recorded signals from the collimator for all shots.

To interpret the result c) we make some considerations. In that range of speed the model predicts fragmentation of the particles impacting on the filter and reabsorption of the ejected fragments in the aluminum foil, i. e. in principle no signals should have been recorded from the collimator. However, it is worth stressing that the model predictions are strictly valid in the regimes below 3 km/s and above 7 km/s. The range between 3 and 7 km/s represents an intermediate territory where a mixed behavior may be observed. Therefore, it is possible that in this range only a partial fragmentation takes place, producing just a limited number of secondary fragments some of which may be still large enough to perforate the rear-wall foil, as also the experiment at TUM described in the previous section showed. However, this was a preliminary test and we did not obtain enough statistics of the shots to draw clear conclusions. These type of tests would require running the accelerator for a longer time as smaller velocities are more probable to be generated from the machine and, as a matter of fact, all the particles generated in case c) did not exceed 7 km/s, meaning that we likely operated very close to the boundary between the two regimes. More tests should be planned for a better understanding of the filter response, although since last year the facility is shut down due to upgrade and relocation. The new facility is expected to become operational in early 2018.

5 Impact risk assessment for ATHENA

The *Advanced Telescope for High Energy Astronomy* [12] is the next large ESA mission dedicated to high energy astrophysics, with a launch planned in 2028. ATHE-NA features an unprecedented ~3 m large *silicon pore optics* (SPO) [13] with two

instruments at the focal plane, the *X-ray Integral Field Unit* (X-IFU) [14], a high resolution spectrometer based on a microcalorimeter array, and the *Wide Field Imager* (WFI) [15], a large size DEPFET-based detector for wide field imaging with high time resolution. Due to the large aperture, micrometeoroids in the interplanetary space may be an issue for the ATHENA focal plane instruments. We did the exercise of calculating the ATHENA effective area for micrometeoroids. As at the time of writing a grazing incidence reflection law measured for the SPO samples is not available, we assumed the scattering density probability measured for an XMM-like gold coated surface [16]:

$$R(\theta) = \left[\frac{1}{0.3} - \left(\frac{\theta}{0.18} \right) \right] \tag{4}$$

We modelled the ATHENA SPO as a Wolter-type telescope with 750 mirror shells, using the parameters reported in [16], i.e. radius varying from 285 mm to 1457 mm, height varying from 20.3 mm to 101.9 mm, and inclination to the optical axis varying from 0.34° to 1.7° (Figure 15). The assumed focal length is 12 m. The X-IFU has been modelled as a dummy detector with 7.5 mm radius, the WFI has been modelled as a dummy detector with 75 mm radius. The analysis evidenced that, while on XMM all mirror shells contribute to the effective area for micrometeoroids, in the configuration assumed for ATHENA only the inner shells do, as shown in Fig. 16. Therefore, despite the fact that the geometrical area of the ATHENA SPO is one order of magnitude larger than that of a single XMM mirror module, the WFI effective area for micrometeoroids results only about twice as large as the XMM effective area, while the X-IFU effective area is about four times smaller than the XMM effective area (Fig. 16). As the XMM
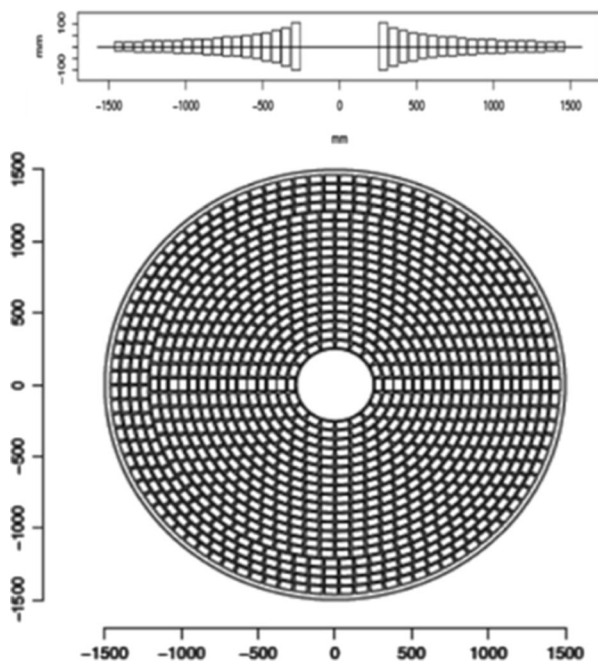

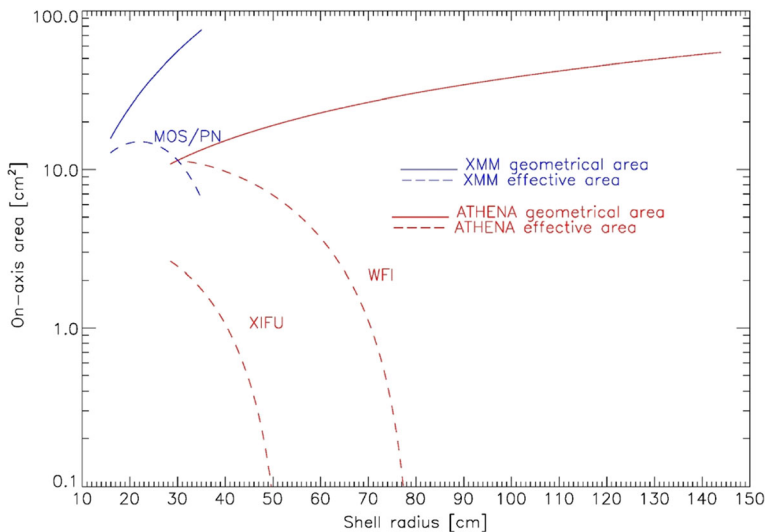**Fig. 15** A drawing of the ATHENA SPO optics (image credits: ATHENA Consortium)

Fig. 16 Differential on-axis geometrical area (solid line) and effective area (dashed line) for micrometeoroids computed for XMM detectors (blue lines) and ATHENA detectors (red lines). An XMM-like scattering law has been assumed here for the ATHENA SPO

average impact-rate of ~0.5 impacts/year corresponds to impacts on an equivalent two mirror module exposed area, we conclude that, assuming that the micrometeoroid flux around L2 is similar to that encountered by XMM (notice that scaling the low earth micrometeoroid flux shown in Figure 1 by a factor ~ 1.4 to get rid of the focussing and shielding effects of the earth gives the so-called Grün flux, i.e. the expected population of micrometeoroids in the interplanetary space, which should be representative of the
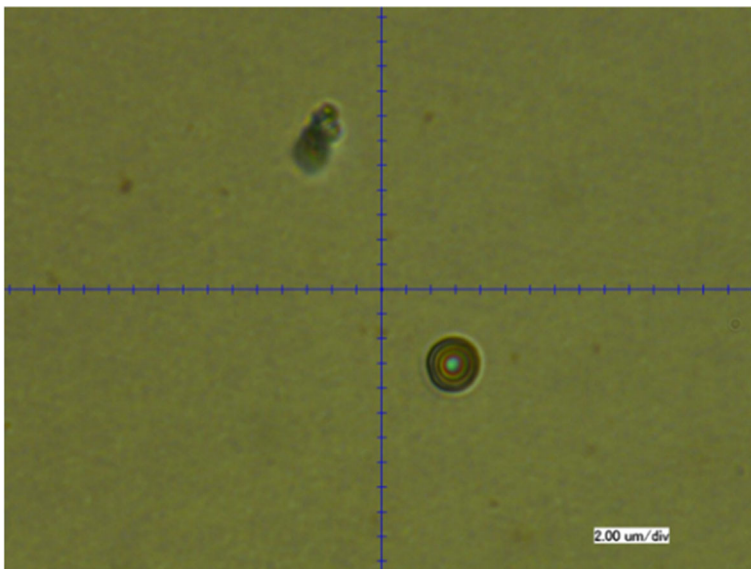

Fig. 17 Crater produced on the SXS HgTe absorber by a hyper-velocity Fe grain with size ~0.5 μm and speed ~5 km/s

environment in the XMM orbit as well as around L2) and that the ATHENA acceptance angle for dust grains is the same as the XMM acceptance angle, we predict for the WFI about the same average impact-rate observed by XMM, while for the X-IFU the average impact-rate would be ~8 times lower, i.e. ~ 0.0625 impacts/year. Although the ATHENA detectors have not been directly tested yet against micrometeoroid impacts, the tests conducted on the LOFT SDD could be to some extent indicative of the type and entity of performance degradation that may be expected for the WFI as well, although, due to the lower energy threshold, the WFI surface passivation is much thinner compared to that on top the SDD. Regarding microcalorimeters, we performed in the past a test campaign on a spare sample of the Soft X-ray Spectrometer (SXS) used on board ASTRO-H, which showed a substantial robustness of the microcalorimeter against hyper-velocity impacts (Figure 17). However, the X-IFU absorbers will be thinner than the SXS ones, therefore they may not be able to withstand so well possible hyper-velocity impacts.

6 Conclusion

We presented an assessment of the risk posed by hyper-velocity impacts to instruments planned on board future X-ray missions. We can summarize our findings as follows:

1) for the LOFT/WFM the risk of damages or failure is considerable, as its large FOV implies that even a few relatively large size grains may reach the SDDs. The optical blocking filter envisaged in the WFM configuration cannot provide enough protection and an additional layer is required to effectively shield the SDDs from these events and make the impact risk low enough. Placing such a rear-wall layer just in front of the SDDs at approximately 20 cm distance from the bumper filter mounted on the coded-mask permits to realize a so-called Whipple shield configuration, whose performance has been investigated by simulations and validated by experimental tests conducted at the plasma accelerator at TUM. The result of this study showed that a 15 μm rear-wall made of polypropylene is capable to effectively stop grains with a few tens micron size, provided that they have a velocity higher than ~5 km/s enabling a complete disintegration on the kapton bumper into a spray of tiny secondary fragments, which then are stopped by the polypropylene rear-wall. The number of grains in orbit with a velocity lower than 5 km/s is expected sufficiently low to neglect the risk posed by them. As for the penetration threshold of the shield at high speed, the maximal momentum we could generate was for grains of ~70 μm size at ~7 km/s speed, which is close to the limit of the accelerator capabilities. However, in the range of parameters achievable with the accelerator our experimental results are in a remarkable agreement with the predictions of the ISS model, that we adopted to simulate the performance in other ranges of the parameter space. The model prediction shows that at a speed of ~10 km/s grains would be stopped up to ~100 μm size, at ~20 km/s up to ~60 μm size. Therefore, according to the expected rate of micrometeoroids larger than ~60 μm and debris larger than ~100 μm reported in Section 3 we estimate a probability of ~60% (at vertical incidence) and ~85% (at 30° incidence) that none of the WFM SDDs will be impacted in the first five years in orbit. Finally, we

stress that the agreement of the ISS model prediction and our experimental data on the prototype shield realized with thin plastic foils is remarkable, considering that the model was derived and previously validated in a quite different context (relatively thick layers made of metal). Indeed, our test provided a validation of the ISS model in a range of parameters that had not been yet explored by experiments. For the LOFT/LAD the risk of a degradation of the effective area due to hyper-velocity impacts is relatively low: only a few particles smaller than 10 μm are expected to hit the LAD SDDs over 5 years in orbit and the optical and thermal filter combined with the silicon oxide passivation on top of the surface can provide some protection. Furthermore, the results of an impact test campaign conducted on SDD prototypes suggest that the detector is quite robust with respect to impacts of micron-sized particles.

2) for eROSITA we simulated and tested the ability of the thin optical blocking filter to disintegrate the smallest micrometeoroids and verified that an external layer coupled to a layer deposited on-chip is advantageous.

3) for ATHENA, despite the much larger geometrical area of the optics a similar impact-rate as XMM may be expected for the WFI, under a number of assumptions: that impacts are due to grains reflected at grazing angles, that the SPO reflectivity is the same as for the XMM mirror shells, and that the micrometeoroid fluxes are the same in the ATHENA and XMM orbits; for the X-IFU, under the same assumptions an impact-rate ~ 8 times lower than that observed by XMM may be expected, due to the smaller size of the X-IFU compared to the WFI. Instead, if the XMM impact-rate was due mainly to secondary ejecta by primaries entering the FOV from any direction, the impact-rate should scale as the geometrical area rather than the effective area, thus for the WFI the impact-rate may be expected much higher than the XMM impact-rate.

References

1. Strüder, L., et al.: Evidence for micrometeoroid damage in the pn-CCD camera system aboard XMM-Newton. A&A. **375**, 5 (2001)
2. Abbey, T., et al.: Micrometeoroid damage to CCDS in XMM-Newton and swift and its significance for future X-ray missions, ESA SP-604, 943, (2005)
3. Smith, D., et al.: Flux and composition of micrometeoroids in the diameter range 1-10 microns. Nature. **252**, 101 (1974)
4. Sørensen, J.: The LOFT radiation environment, ESA report, (2012)
5. Langwost, A., et al.: Presentation of the PC version of the ESABASE/debris impact analysis tool, ESA-SP-578, 619, (2005)
6. Feroci, M., et al.: The large observatory for x-ray timing, Proc. of SPIE, 8443, 8443-2D, (2012)
7. Zane, S., et al.: The large area detector of LOFT: the Large Observatory for X-ray Timing, Proc. of SPIE, 8443,8443-2F, (2012)

8. Brandt, S., et al.: The LOFT Wide Field Monitor, Proc. of SPIE, 8443, 8443-2G, (2012)
9. Igenbergs, E., et al.: The TUM/LRT Electromagnetic Launchers. IEEE Trans. on Magnetics. **22**(6), 1536 (1986)
10. Zampa, G., et al.: The effects of hyper-velocity dust-particle impacts on the LOFT Silicon Drift Detectors, JINST,9, P07015, (2014)
11. Predehl, P., et al.: eROSITA on SRG, Proc. of SPIE, 9144,9144-1T, (2014)
12. Nandra, K., et al.: The Hot and Energetic Universe: a White Paper presenting the science theme motivating the Athena+ mission, arXiv:1306.2307, (2013)
13. Willingale, R., et al.: The Hot and Energetic Universe: The Optical Design of the Athena+ Mirror, arXiv:1307.1709, (2013)
14. Barret, D., et al: The Hot and Energetic Universe: The X-ray Integral Field Unit (X-IFU) for Athena+, arXiv:1308.6784, (2013)
15. Rau, A., et al.: The Hot and Energetic Universe: The Wide Field Imager (WFI) for Athena+, arXiv:1308.6785, (2013)
16. Meidinger, N., et al.: Experimental Verification of a Micrometeoroid Damage in the PN-CCD Camera System aboard XMM-Newton, Proc. of SPIE,4851,243, (2003)